DESIGN, MANUFACTURING AND TESTING OF HIGHLY INSTRUMENTED ROTOR BLADES FOR A MEDIUM SIZE HELICOPTER WIND TUNNEL MODEL

Henning Mainz [1)], Oliver Schneider [1)], Rainer Bartels [1)], Bram van de Kamp [2)]
German Aerospace Center (DLR)
1) Institute of Flight Systems, Braunschweig, Germany
2) Institute of Lightweight Systems, Braunschweig, Germany

Abstract

At DLR Braunschweig, a new four-bladed medium size helicopter wind tunnel test rig on a scale of 1:6.375 to the EC-135 was manufactured and tested in the framework of DLR´s guiding concept "The Rescue Helicopter 2030". This paper deals with the design and manufacturing of new hingeless Mach-scaled rotor blades and the interaction between structural aspects and the dynamic behavior. It deals specifically with the challenges and particularities of composite rotor blade manufacturing of relatively small, highly instrumented rotor blades with pressure sensors and strain gauges. Test results and an assessment of a single blade as well as test results of the whole rotor on DLR`s test rig are presented.

1. INTRODUCTION

At DLR`s (German Aerospace Center) facility in Braunschweig, three different mobile rotor test rigs are available. The MWM (Modular Wind Tunnel Model) is a modularly designed device suited to investigate Mach-scaled helicopter configurations with different main rotors, rotor hubs and fuselage shells. It allows the operation of an additional tail rotor system with different blade sets. Main and tail rotors are hydraulically driven and have a rated power of up to 135 kW or 12 kW, respectively. ROTEST (ROtor TEst STand), the second test rig with a generic fuselage is designed for isolated rotor research capable of a nominal power output of up to 190 kW. The main rotors examined on ROTEST typically have diameters between 4 m and 4.2 m. Most of the rotor blades investigated in the past were manufactured at DLR (**Reference 1, 2, 3**).

To gain further capabilities in wind tunnel testing, now a third medium-sized model with a rotor diameter of 1.624 m was designed and manufactured for use in smaller wind tunnels like the DNW-NWB (Low-Speed Wind Tunnel Braunschweig) with a cross section of 3.25 m x 2.8 m. This new model is therefore called NWB-Model in the following. Within the context of DLR´s project "Fast Rescue", two different fuselages without rotor (the rotor system was not yet operational) were tested at DNW-NWB in 2020. First, a reference configuration similar to an EC-135 was tested (see Figure 1).

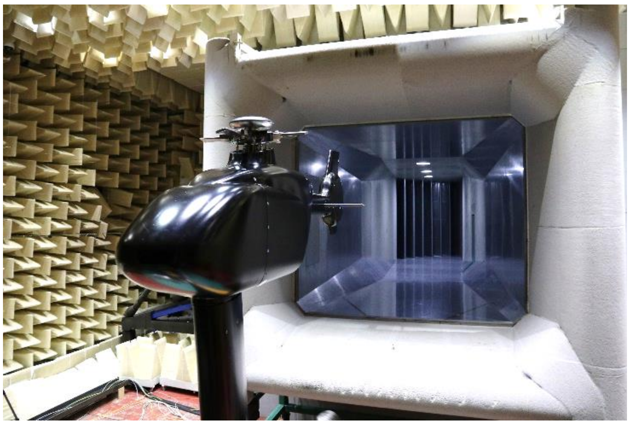

Figure 1: Reference fuselage configuration at NWB

This test was followed by the investigation of the newly developed optimized fuselage SZ1 (Scenario 1) with v-tail which is shown in Figure 2.

Figure 2: SZ1 fuselage configuration

Further investigations with a complete rotor system and stub wings were carried out in the context of DLR´s project “Urban Rescue” which resulted in a wind tunnel test in June 2024. This involved the completion of the rotor head, the blade control system and the manufacturing of the rotor blades. The latter is the main topic of this paper.

In addition to the three test rigs, a whirl tower for rotors with a radius of up to 2.5 m is also available on site for blade laboratory tests and for icing or deicing tests.

2. NWB-MODEL

In order to prevent too much blockage of the flow and influences from wind tunnel walls, the rotor diameter should roughly be half the test section width. The NWB wind tunnel test section size is 3.25 m x 2.8 m. Thus, a rotor diameter of approximately 1.6 m was chosen. The reference helicopter configuration is based on an Airbus Helicopters EC-135 with a rotor diameter of 10.2 m. Thus, the initial model scaling factor was 6.375. To appropriately account for aerodynamic and aero-acoustic phenomena, Mach scaling is used for the rotor system. During the design of the model, it turned out that more installation space was required for some rotor head components. So, with the same blade geometry, the rotor diameter was increased by 1.5%. The final model properties are shown in Table 1.

Table 1: Main model properties

	Symbol / unit	value
Rotor diameter	R / m	1.624
Tip speed	v_{Tip} / m/s	211
Angular velocity	ω / rad/s	260
Rotor speed	n / rpm	2481
Tip Mach number	Ma_{Tip} / −	0.615
Nominal thrust	T / N	724
Blade mean chord	c / mm	57
Desired rotor power	P / kW	50
Rotor system		hingeless
Sense of rotation		counter-clockwise
Attachment		belly sting

Figure 3 shows an x-ray view of the NWB-Model in the SZ1 fuselage (1) configuration with belly sting, sting fairing (2) and stub wings (3).

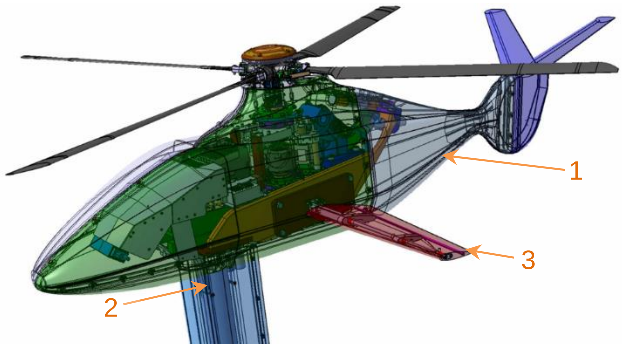

Figure 3: SZ1 with stub wings

Figure 4 gives a more detailed view of the inner structure of the model. A hydraulic motor (4) drives the rotor shaft and thus the rotor head (5) via a toothed belt transmission (6). The drive and rotor are mounted on a frame which is bolted to the sting connection flange (7) at the front of the model via a rotor balance (8). The fuselage shell is connected to a cylindric fuselage balance (9). Through a separate frame (10) the non-measuring part o*f this balance is also bolted to the model sting connection flange. The wings contain wing balances (11) that are connected to the latter frame. This ensures* that all balances measure independently from each other. A detailed description of the model can be found in **Reference 4**.

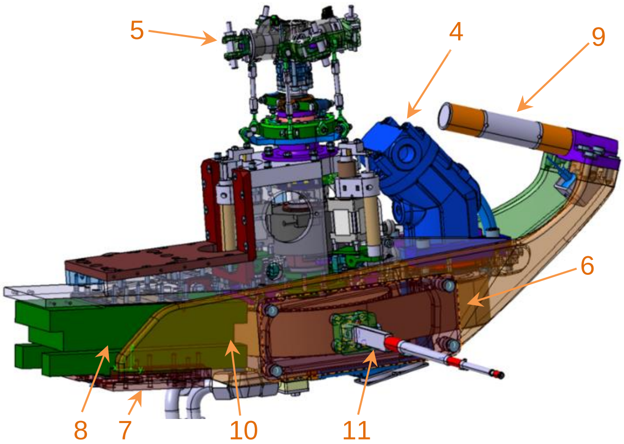

Figure 4: Model inner structure

3. BLADE DESIGN

3.1. Blade geometry

For the NWB-Model rotor blade, the 7AD (**Ref. 5**) rotor is the reference configuration. The 7AD rotor blade has a rectangular shape with a parabolic swept back blade tip and a straight trailing edge. Furthermore, the tip has an anhedral angle which is not implemented for the NWB-Model rotor. The root (blade neck) and clamp area (loop) are derived and scaled from a Bo105 model rotor blade. The blade root operates as an elastic flap and lead-lag hinge whereas the friction of the spar loop between the blade and the blade clamping device acts as a lead-lag damper. Figure 5 shows the outer blade geometry with the loop (1), the blade neck (2), the transition zone (3) and the aerodynamic part with parabolic blade tip (4).

Figure 5: Outer blade geometry

The experiences and design from the FTK-META (Fortschrittliche Taumelscheiben Konzepte – Mehrfachtaumelscheibe / Advanced Swashplate Concepts – Multiple Swashplate; **Ref. 2**) project are incorporated as a starting point for the NWB-Model rotor blade design, especially regarding the blade loop and root.

3.2. Scaling requirements

The downscaling poses higher demands to the manufacturing, because tolerances scale accordingly and the inner structures get very delicate.

A Mach-scaling is necessary to account for aerodynamic and aero-acoustic phenomena. This results in a rated rotational speed of the rotor blade of 2481 rpm and a blade tip speed of 211 m/s, accordingly. Several different scenarios are investigated. Therefore, the operating rotational speed varies between 50% for the "slowed rotor" and 115% for “high-speed impulsive noise". Dynamic similarity to the original blade is not envisaged because this would lead to instabilities in the “slowed rotor” mode. Nonetheless, dynamic stability is a major aspect to be regarded for design and dimensioning of the rotor blade.

To account for Reynolds number effects, the chord length is increased by 12%, which increases the rotor solidity by the same amount. The chord length is 57 mm.

Due to the very wide range of operating conditions, particular attention had to be paid to the dynamic design of the blades. The placement of the non-dimensional natural frequencies of the blades must ensure dynamically safe operation of the rotor over a wide rotational speed range. Normally, while scaling rotor blades to model scale, the aim is to match the dynamic characteristics of full-scale blades. For the NWB-Model blades this is not the case. The usual approach is to place the blade natural frequencies such that in the Campbell diagram, there are no intersections with the multiples of the rotor rotational frequency in the relevant rotational speed range. Unfortunately, these intersections cannot be avoided for the desired large variation of the rotor rotation frequency. Consequently, the final dynamic blade design can only be a compromise and may not fulfill all requirements.

To calculate the dynamic characteristics, a data set of the structural properties of an equivalent beam model for the NWB-Model rotor blade was set up and used for the calculation by a finite element program. The starting point for the dynamic design was a mixture of structural properties of similar scaled 2D-sections from existing blades (Bo105, FTK, 7AD).

Based on this initial blade design, an iterative process between the analysis and the modification of the data set with a consistent refinement of the 2D-sections and improvement of the results in terms of the objected target frequencies is necessary (see section 3.5).

After the iterative process is finished, the structural properties of the beam match the properties of the inner structure, and the natural frequencies of the blades are well placed. The rotor Campbell diagram of the final design step is shown in Figure 6. Due to the high demands on the operating conditions, the resulting blade is stiff-inplane, i.e., the non-dimensional first lead-lag frequency at nominal rotor speed is larger than 1/rev. At nominal rotor speed, all presented natural frequencies (flap F1-F4, lead-lag L1-L2, and torsion T1) keep a distance of at least 0.2/rev to the multiples of the rotational frequency. Thanks to the beneficial design of the blade's inner structure, there are also no couplings between the bending or torsional modes over the complete rotational frequency range. The crossings of the first lead-lag natural frequency with the second rotor harmonic at about 0.75 Ω_{ref} and with the third rotor harmonic at 0.5 Ω_{ref} are critical. The operation of the rotor at these rotational frequencies must be avoided.

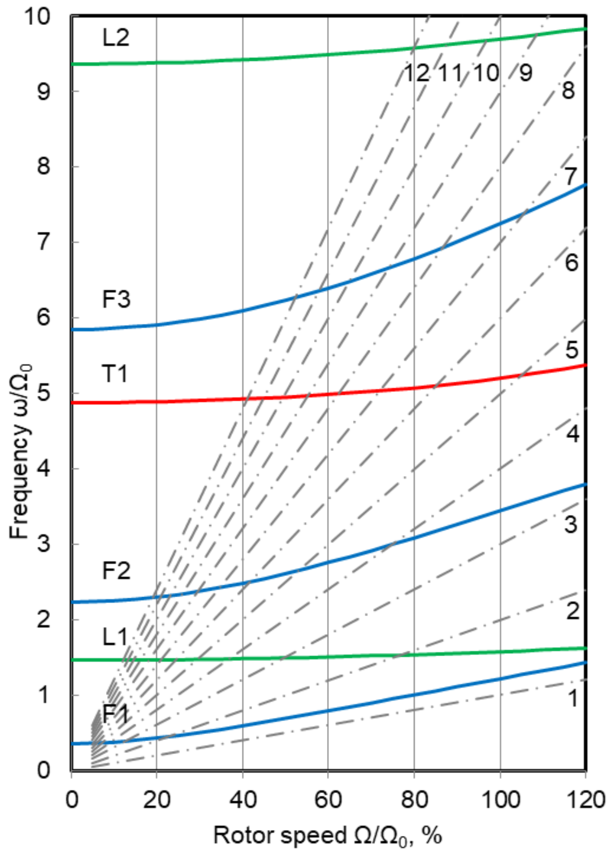

Figure 6: NWB-Model rotor Campbell diagram

3.3. Blade hull

The blade hull design features the aforementioned scaled 7AD aerodynamic part and the root section similar to that of the Bo105. The main parameters for the aerodynamic part are the chord length, the airfoil (OA2xx series) and twist distribution. The construction is based on a section-wise design, which is important to modify the inner structure design. The sections are connected with tangentially continuous surfaces. The number and positions of these sections depend on the radial airfoil changes. The quality of the outer surface has been checked by isophote analysis. Figure 7 shows very smooth isophote lines, proving the tangential continuity. Stronger changes in their course can only be seen in the airfoil transition regions.

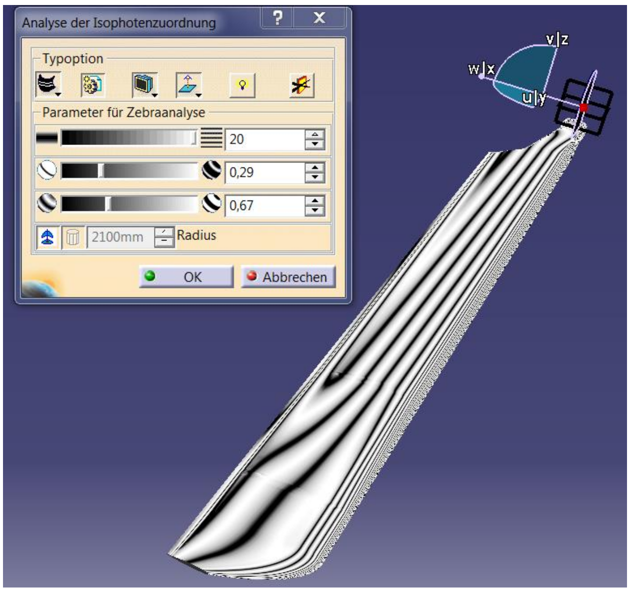

Figure 7: Isophote analysis

3.4. Blade inner structure

As pointed out in **Ref. 1**, the inner geometry is depending on the blade hull geometry. This predetermination of the outer hull forces a design and construction process from outside to inside. The main parts of the rotor blade are the skin as the outer hull, a spar (carbon fiber reinforced plastic, CFRP) to carry most of the loads, a foam core to support the skin and a nose counterweight to position the center of gravity (Figure 8).

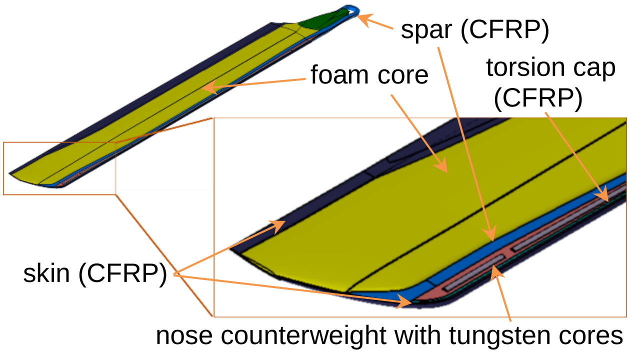

Figure 8: Aerodynamic blade part inner structure

All these parts are highly interdependent. The same cross sections as for the outer hull are important to account for the interior geometric changes. Additional cross sections are necessary for the 3D-design of the inner structure because of the complex geometries resulting from boundary conditions like directional stiffness distribution, strength demands, geometric continuity, manufacturing requirements, material properties and the position of the center of gravity.

Major aspects with high impact on the design are the center of gravity, the load distribution and the blade root's directional stiffness. The center of gravity is important for the aero-elastic stability of the rotor blade and causes demanding geometrical restrictions. For aero-elastic stability, the center of gravity of the rotor blade should be located at about 25% chord length or slightly in front of it. Especially the blade root determines – in combination with the load distribution – the dynamic behavior of the blade and has to endure the highest loads. To tailor this behavior and strengthen the blade to withstand all loads, material choices had to be changed and additional material layers and a short fiber core have been integrated (Figure 9).

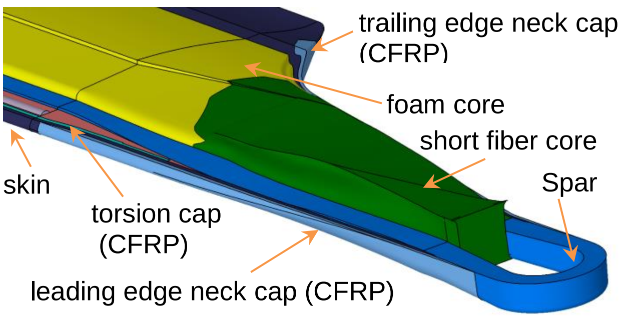

Figure 9: Blade root inner structure

Initially, the spar was planned as a glass fiber reinforced plastic (GFRP) spar, similar to the FTK-META rotor blade for which S-glas fibers were used to achieve some additional stiffness and strength. For the NWB-Model blade, the dynamic properties were not satisfying. Thus, the final blade design relies on a CFRP-spar.

3.5. Structural analysis and iterative design process

To align all these partly contradictory requirements addressed in section 3.4, an iterative process of geometry design and structural analysis is necessary. Since this paper focusses on the manufacturing, only the results of the final structural and strength analysis will be shown and briefly be discussed. The design and analysis process are not shown in detail. A description of a similar design process can be found in **Ref. 2**. The development and automation of tools has also been a part of research in the DLR rotorcraft community (for example **Ref. 6**). Also, the SaMaRA - Structural Modeling and Rotor Analysis Code (**Ref. 2**) has been updated. It determines the section-wise structural blade properties of a rotor blade and is now more robust and much faster than before.

4. BLADE MANUFACTURING

Helicopter manufacturers usually produce their series rotor blades using a hot process with prepregs. Prepregs are fiber materials pre-impregnated with resin (fiber volume content 60%) with very good fiber orientation, which require hot curing, usually at 120°C to 180°C. Prepregs can be used to produce large quantities of high-quality rotor blades preferably in a single shot, i.e., comparatively quickly.

As we only need four rotor blades plus a spare one, and a very high fiber volume content is not important, we decided to use dry fiber material that has to be resinated with cold-curing resins. This achieves fiber volume contents of around 50% and, depending on the resination method, very good results. Difficulties with hot curing due to different thermal expansion coefficients between blade material (fibers) and mold material (in our case aluminum) during the blade manufacturing process are avoided. A cold process is easier to handle, the requirements for the molding are lower and it is very well suited for blade construction in several steps as it is done here.

4.1. Skins

Two negative mold halves are required for the manufacturing of the rotor blades, in which the upper and lower skins are created. These molds (Figure 10) are also used to assemble the blades.

Figure 10: Aluminum negative molds

The skins were produced using the RTM (Resin Transfer Molding) method. This is a low-pressure closed molding process, which offers a good surface finish product. It starts with the following mold preparation tasks:

- Coating the molds with release agent.
- Masking the mold areas that should not come into contact with resin with suited tape.
- Mounting of 3D printed raised edges for tangential layer run-outs (avoids sharp bending of the layer overlaps).
- Gluing in the SPR (Stereo Pattern Recognition → optical blade deformation analysis) dots with spray adhesive.

Figure 11 shows the mold halves after the described preparation works before fixing the fiber material layers. Here you can see the brown masking tape, the SPR dots and the grey raised edges

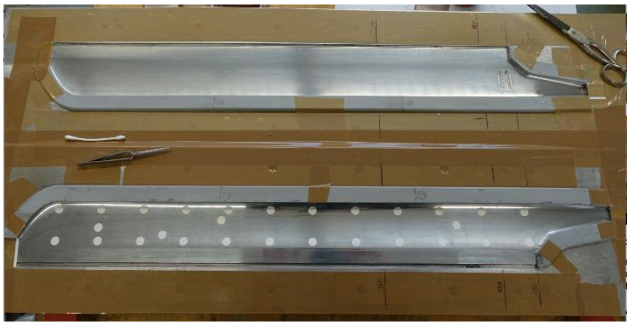

Figure 11: Mold preparation

Each mold is now equipped with a layer of thin glass fiber fabric (leads to a good blade surface) followed by four layers of carbon fiber fabric of different lengths and orientation. Spray adhesive ensures that the layers adhere to the mold and to each other. This step is shown in Figure 12.

Figure 12: Mold halves with fiber material

Figure 13 shows the completed preparations for the resin infusion. A tear off sheet (1) consisting of several parts covers the fiber material and partially the molds. Now a perforated separating film (2) is placed between the tear off sheet and the resin flow aid (3). Absorbent fleece (4) is located under the vacuum line (5) and the vacuum measuring line (6). It serves as a resin flow decelerator.

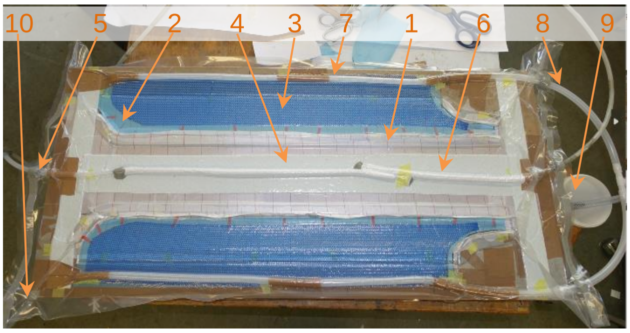

Figure 13: Completed infusion preparations

In the mold area both vacuum lines consist of spirals which are covered by semipermeable hoses which let air through and repell resin. This protects the pump and the manometer from resin. Two spiral lines (7) positioned at the outer edges of the molds lead into tubes (8) which are connected to another hose via a T-piece. The latter is in the resin reservoir (9). A transparent vacuum hose is used to seal the areas around the molds airtight (10).

Now while the resin line remains closed the fiber material is evacuated by means of a vacuum pump. After this the resin line is opened and the resin flows into the cavities. Figure 14 shows the infusion after clamping off the resin supply.

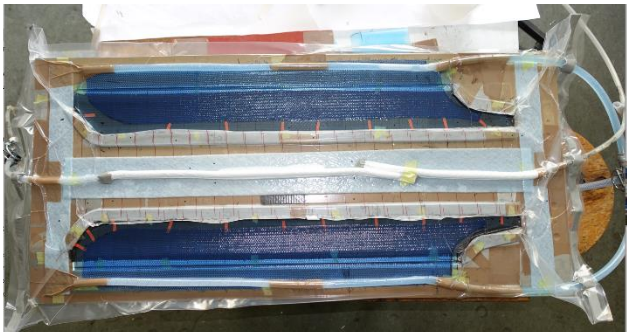

Figure 14: Finished resin infusion

The vacuum pump runs until the resin is cured.

All auxiliary materials are removed after 24 hours. Protruding fiber composites are cut off and the molds are freed from resin residues. What remains are the rotor blade skins in their mold halves (Figure 15).

Figure 15: Upper and lower blade skin

4.2. Instrumentation and blade tip LED

4.2.1. Strain gauges

The rotor blades are equipped with a torsion strain gauge bridge at 30% blade radius and 25% chord length. These are glued in with either superglue or resin. Figure 16 shows a torsional strain gauge glued into an upper skin. It looks the same in the lower skin. Four cables are then soldered to the soldering terminals.

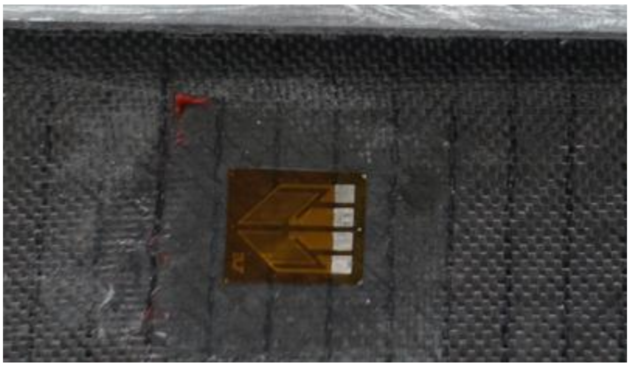

Figure 16: Glued in torsional strain gauge

4.2.2. Blade tip LED

Adjusting the tracking of a rotor is always a challenge, especially if the tips of the blades are very small, as in our case. Small LEDs, already fitted with cables, were therefore glued into the upper blade skin to ease the detection of the blade tip motion. Figure 17 shows a glued-in and illuminated rotor blade tip LED.

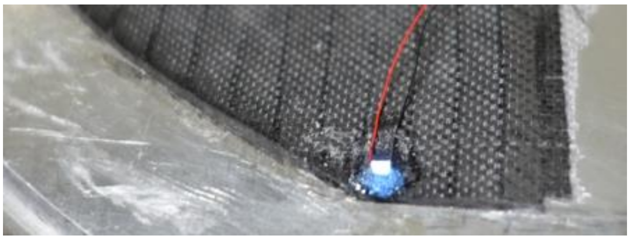

Figure 17: Blade tip LED

4.2.3. Pressure sensors installation

Blade 1 is to be fitted with 14 high frequency pressure sensors at 70% radius. An iteration between the aerodynamically desirable sensor positions and the constructionally feasible sensor positions with regard to the available installation space resulted in the sensor distribution shown in Table 2. The upper side of the blade features eight sensors between 2% and 80% chord and the lower side six sensors between 2.5% and 80% chord.

Table 2: Pressure sensor distribution

upper side								
No.	1	2	3	4	5	6	7	8
R [%]	69.8	70	70	70	70	70	70	70
x [%]	2	5.5	10	18	28	42	61	80
lower side								
No.	9	10	11	12	13	14		
R [%]	70.2	69.2	70	70	70	70		
x [%]	2.5	5.5	10	28	51.5	70.5		

Due to the lack of space, three pressure sensors in the blade's nose area have to be installed at a small offset from 70% R. Figure 18 shows this situation.

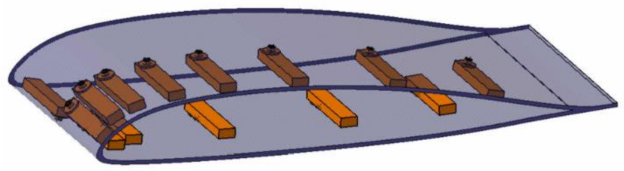

Figure 18: Pressure sensor distribution at 70% radius

Kulites of type LL-32A-072-25A are to be installed into the rotor blade. Figure 19 gives an impression of the size of such a pressure sensor in comparison to a metric ruler. These flat sensors have a chimney-like tube above the measuring point, which must pass through the blade skins to the rotor blade surface. Each sensor is fitted with four cables (2) of the size AWG38 (Ø 0.22 mm).

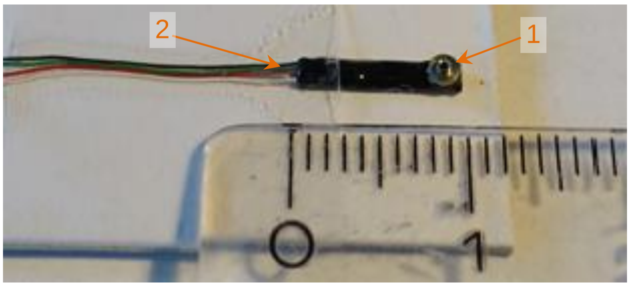

Figure 19: Kulite LL-32A-072-25A

The sensors are glued in using epoxy resin. To position the sensors correctly, holes of the size of the sensor chimney (0.9 mm) must be drilled into the skins. For this purpose, a template was produced using 3D resin printing, which guides the drill bit when drilling the holes. Figure 20 shows the drilling template (1), which was clamped (2) above the upper carbon fiber skin (3) in the aluminum mold (4) at 70% radius. The drilling tool is in the background (5).

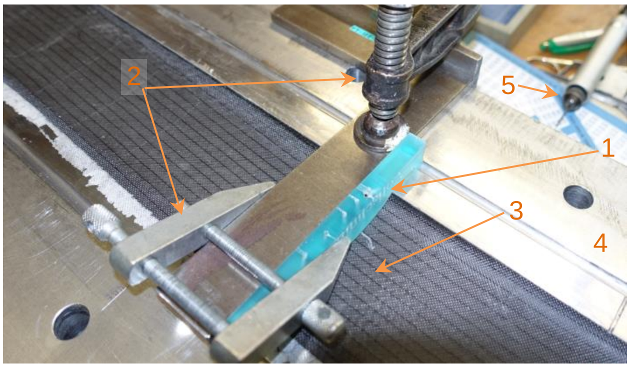

Figure 20: Sensor hole drilling preparation

In order to drill completely through the skin, the drill must penetrate the mold slightly (Figure 21).

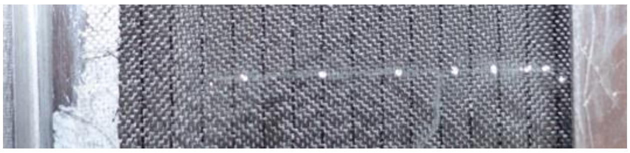

Figure 21: Upper blade skin with sensor holes

Now the sensors are inserted one by one into their holes and glued in with epoxy resin. The auxiliary device shown in action in Figure 22 was used for this process.

Figure 22: Gluing in a pressure sensor

After all the sensors were glued in place, they were completely covered with epoxy resin (Figure 23).

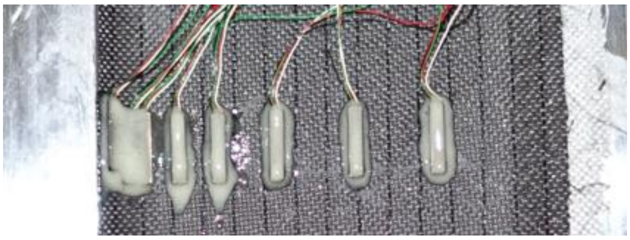

Figure 23: Pressure sensors inside the upper skin

The lower skin was fitted with six sensors. Figure 24 shows how the sensors were arranged according to the space constraints.

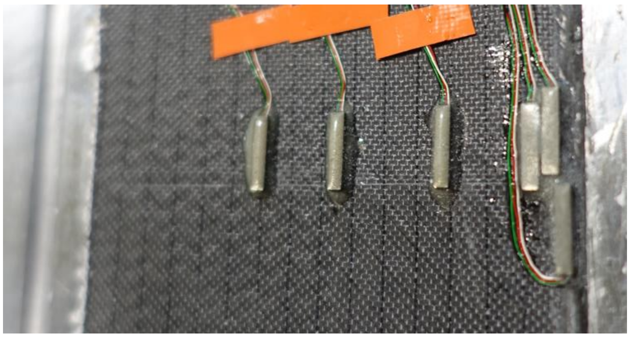

Figure 24: Pressure sensors inside the lower skin

4.3. Torsion lid and nose counter mass

The CFRP lid connects the nose section of the upper and the lower skin in order to reach a torsionally stiff connection between both parts. It extends to nearly the whole aerodynamic part – except the parabolic blade tip – and was made by hand using 3D printed molds. Figure 25 shows a rotor blade cross-section with the torsion lid (1) in front. The inner area contains tungsten rods 14 x 2 mm (2) at a distance of 1 mm from each other, which are embedded in a mixture of tungsten powder and epoxy resin (3).

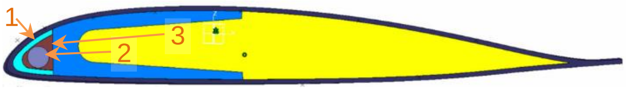

Figure 25: Rotor blade cross-section

The tungsten rods were omitted in the area of the pressure sensors as they would collide with the sensors.

All nose mass caps for the blades without pressure sensors have been trimmed to the same mass and center of gravity. Figure 26 shows a nose mass cap during the center of gravity determination.

Figure 26: Nose mass cap center of gravity determination

The nose mass cap for the blade with pressure sensors was specifically trimmed to compensate for the additional weight of the sensors and cables, so that the blade with pressure sensors has the same mass and the same center of gravity as a blade without pressure sensors. In the area of the pressure sensors, the nose mass cap had to be completely removed to provide the required clearance for the sensors. Thus, it now consists of two parts.

Now the nose mass cap, which consists of the torsion lid, the tungsten rods and the tungsten powder resin mixture, is glued into the upper blade skin with epoxy resin. While curing, it is positioned with the help of 3D printing templates and fixed in place with screw clamps (Figure 27).

Figure 27: Gluing in the nose mass cap

Figure 28 shows the upper skin (1) with the two parts of the nose mass cap (2) glued in place and the gap between them in the area of the pressure sensors (3).

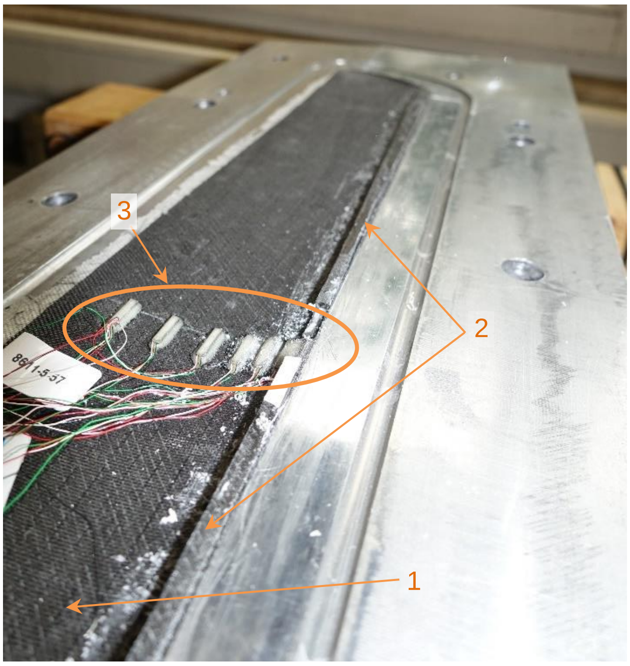

Figure 28: Upper skin with nose mass cap

The free space that is still visible is taken up by the sensors of the lower skin when the blade is assembled.

4.4. Internal wiring

Figure 29 shows the initial state of the cabling in the lower blade skin. A bundle of cables must be routed from the sensors (2) to the cable exit point on the blade neck (3). On the upper side it looks quite similar.

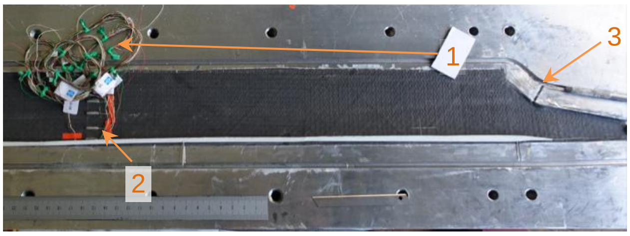

Figure 29: Lower skin cabling – initial state

Six pressure sensors are installed in the lower shell. This means that 24 cables must be laid. Two cables are necessary for the power supply of the LED at the blade tip and four cables are connected to the strain gauges. All 30 cables were laid next to each other. No cables cross one another except in the area of the cable outlet. Figure 30 depicts the almost completed cabling of the lower shell of the blade. All cables were glued in using fast curing epoxy resin. They are routed around the torsion strain gauge (1) the cables of which are then included in the cable harness.

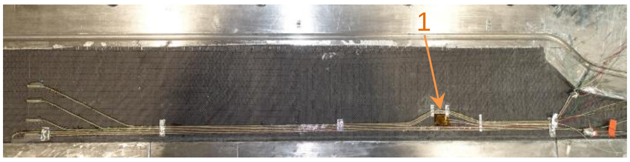

Figure 30: Lower skin cable layering

The wiring of the pressure sensors on the upper side is laid in a different way. Here (Figure 31), the 32 cables coming from the pressure sensors are routed flat from the pressure sensors to the nose mass cap (1).

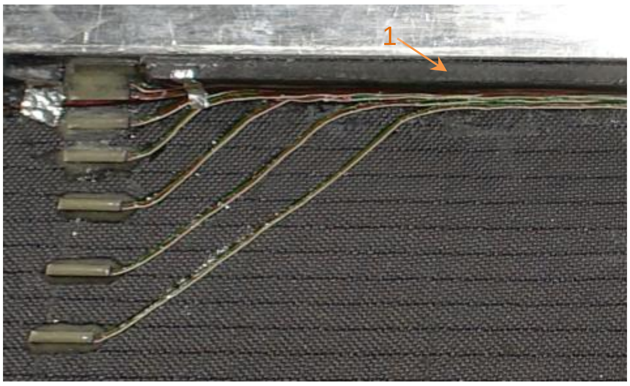

Figure 31: Cable routing in the area of the pressure sensors

From this point, all cables (incl. two LED power supply and four strain gauge cables) run in a bundle along the nose mass cap. Figure 32 shows the cable route from the nose mass (1) to the cable exit point (2). To minimize disruption to the inner blade structure, the cable bundle (3) is transferred into a flat cable tape (4).

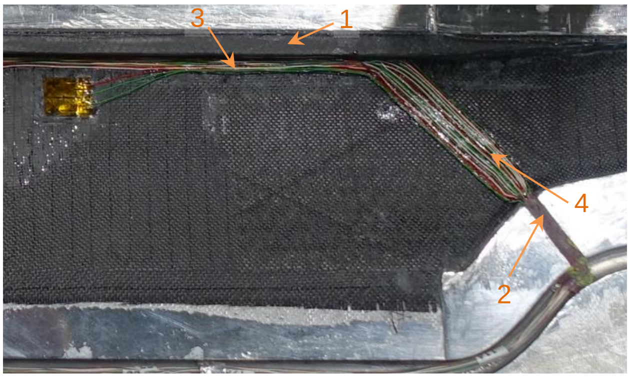

Figure 32: Cable routing to the exit point

4.5. Foam

The production of the foams for the blades is challenging, as they have to be milled from all sides. A vacuum bed was used for this. First, one side of the foam was milled from a rectangular block. Then the foam was turned over and placed with the milled side in the appropriate mold so that the other side could be milled. Figure 33 shows the CAD model of the milling table (1), the vacuum bed (2), the foam milled from a rectangular block (3) and the final foam (4). Figure 34 shows a milled foam from the upper and lower side.

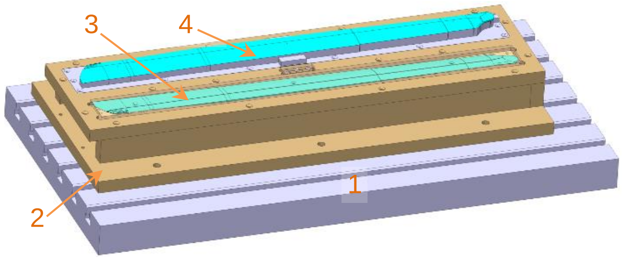

Figure 33: Foam manufacturing device

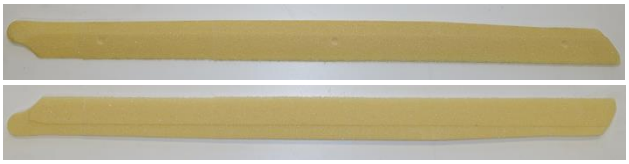

Figure 34: Top and bottom view of the foam

4.6. CFRP spar

The main function of the spar is to carry the centrifugal loads. In such a one-dimensional load case, unidirectional fibers are the best choice. Rovings – these are bundles of single fibers (Figure 35) – are used here, which are impregnated with resin in a pultrusion device.

Figure 35: Carbon fiber roving

Figure 36 shows how the rovings are impregnated in principle. The rovings (1) coming from above run around a central roller (2). Two spring-loaded pressure rollers (3) press the rovings against the central roller. A hose pump (4) supplies resin from the resin tank (5) to the central roller and the right-hand pressure roller. This creates a resin bath (6) in which the rovings are soaked. With the help of a winch, the rovings are pulled through the device. At the outlet of the device (7), a fiber tape consisting of several rovings is obtained.

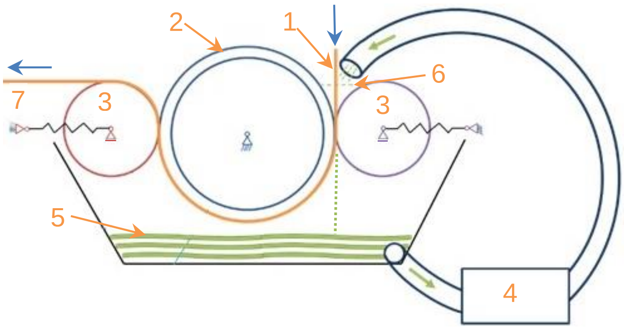

Figure 36: Sketched roving pultrusion device

A fiber volume content of around 50% can be set with the help of the spring preload and the winch speed.

Figure 37 shows the roving impregnation device in action. In this case three rovings (1) are fed in to produce a roving tape. Next to the central roller (2) are the pressure rollers (3), which can be pre-loaded via a double spring and lever mechanism (4). The impregnated rovings run over a guide roller (5, not shown in Figure 36) and are pulled through a set of rollers (6) with which the thickness and width of the roving tape (7) can be adjusted.

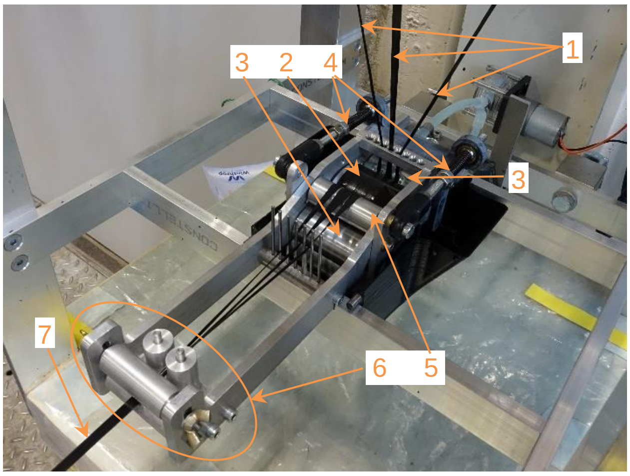

Figure 37: Roving pultrusion device in action

Several of these tapes are used to build up the spars of the rotor blades. From a technical point of view, the outcome of the pultrusion procedure are prepregs.

The spar forms a loop at the blade root. In the transition to the aerodynamic blade area, the spar is transformed into a c-shape. Half of the spar is built up in the lower shell and the other half in the upper shell.

Figure 38 shows the shape of the upper half of the spar with the loop (1), the transition to the c-spar (2) and the fully developed c-spar (3) of the aerodynamic blade area.

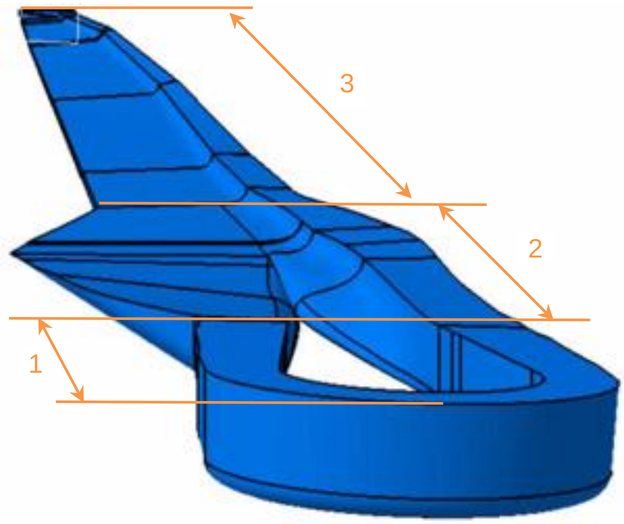

Figure 38: Shape of the upper half of the spar

The loop has an almost rectangular cross section which crosses over to one half of a c-shaped spar in the aerodynamic blade section. The spar half consists of six carbon fiber tapes which have to be guided and distributed in a certain way. In the loop area, each half spar consists of all six roving strips. Three of them reach to the tip of the blade, while the other three end within the blade. The crucial area is the cross over from the loop to the aerodynamic blade section where the CFRP tapes are turned from vertical to horizontal orientation. This process is shown in Figure 39 for the first tape of one half of the spar. For better visibility of the process, a picture of another rotor blade manufacturing with a glass fiber tape was chosen instead of the actual carbon fiber tape.

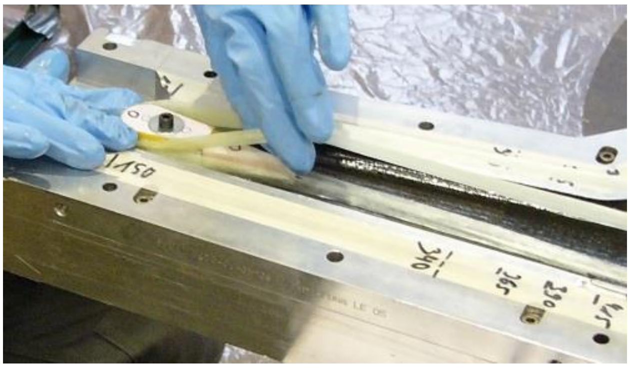

Figure 39: Glass fiber tape during deposition (other rotor blade with glass spar instead of carbon spar shown)

4.7. Blade assembly

To assemble a rotor blade, its components are set up on a table as shown in Figure 40 and the following tasks have been completed.

- Upper (1) and lower (2) skins are completed with sensors and wiring.
- A nose mass cap (3) is glued into the upper skin.
- A removable nose mass dummy (4) is inserted into the lower skin as a boundary for the half spar manufacturing.
- Removable spar rear edge guide bars (5) are inserted into the skins.
- The foam (6) is finished.
- All templates and spar inspection jigs (7) are prepared.

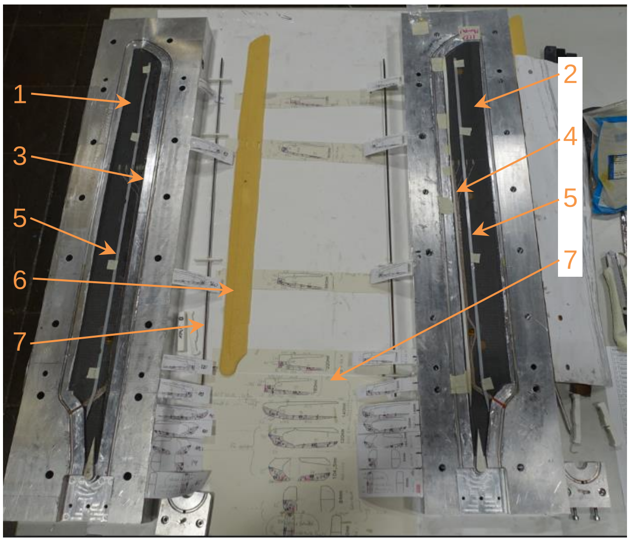

Figure 40: Blade assembly preparation

The roving pultrusion machine is now put into operation and the required quantity for the production of the spar plus some spare of roving tapes are produced. Figure 41 shows the placing of a roving tape starting from the root loop.

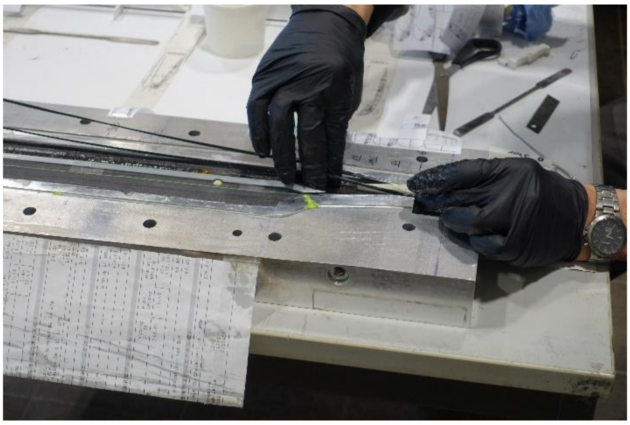

Figure 41: Placing a roving band

Each half spar is gradually created according to a laying and cutting plan. When the tapes have been laid to form a half spar, its shape is checked with templates (1) and adjusted if necessary (Figure 42).

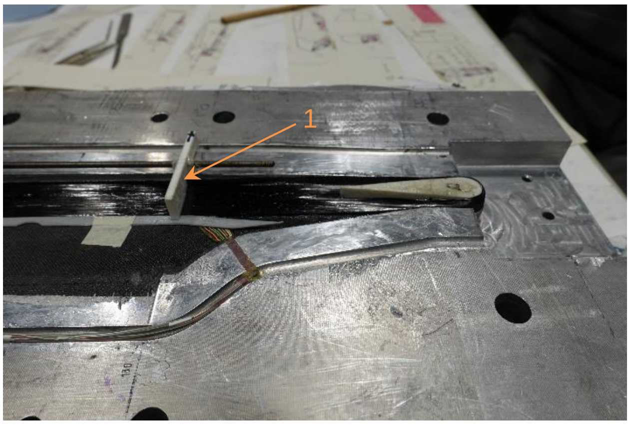

Figure 42: Checking the upper half of the spar

Now all auxiliary devices are removed, the blade root area is filled with thickened resin and the foam is inserted into the lower shell (Figure 43; nose mass dummy is removed directly before assembly).

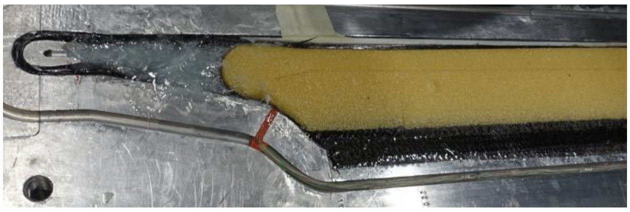

Figure 43: Bottom shell final preparation before assembly

Figure 44 shows the final assembly preparation of the root area of the upper skin.

Figure 44: Upper skin with thickened resin

The two mold halves are now merged (Figure 45) and screwed together.

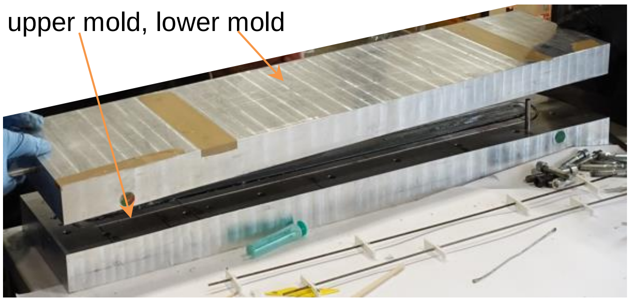

Figure 45: Closing the mold

4.7.1. Thermal treatment

In order to reach the final composite properties, a thermal treatment is required. This happens inside a styrofoam box. Heating mats were used to heat the closed mold. Four temperature sensors which were placed on the mold were used to control the temperature. The temperature cycle requires a slow heating up to 55°C. This temperature is maintained for at least 16 hours before being slowly cooled down again.

4.7.2. Demolding

Once the blade is cured, the two halves of the mold are separated from each other. Figure 46 shows the rotor blade lying in the lower mold.

Figure 46: Rotor blade in the lower mold

The blade is then removed from the mold. After the removal of excess resin and excess material, the blade looks like shown in Figure 47.

Figure 47: A neatened rotor blade

4.8. Blade neck caps

In the aerodynamic blade area, the torsional connection between the upper and the lower shell is achieved by the nose mass cap which is glued into the blade. In the blade neck area, this is achieved by carbon fiber layers glued on from the outside. Before the layers of the blade neck caps are glued on, the subjacent surfaces must be sanded. The areas of the blade that are not to come into contact with the resin are masked with tape. The resin-impregnated layers are pressed onto the blade neck with the help of two pressing tools (Figure 48).

Figure 48: Pressing on the blade neck cap layers

The thickness of the blade neck caps was considered when designing the blade mold. Thus, after sanding the fiber layers a smooth transition is obtained (Figure 49). A shrink tube (1) protected the blade cables from the resin during the gluing process.

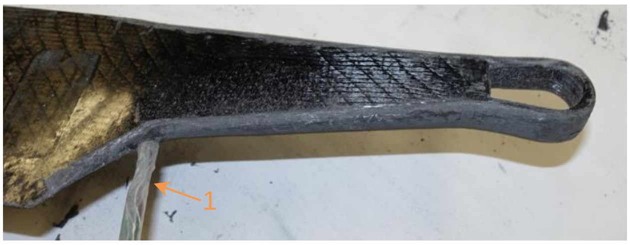

Figure 49: Blade neck with blade neck caps

4.9. Blade shoe mounting

For mounting the rotor blades to the rotor head, a blade shoe is necessary. Supported by a special rack, the loop of each blade is glued into the aluminum blade shoe (Figure 50).

Figure 50: Blade shoe mounting

4.10. External strain gauges and wiring

To monitor the rotor blade loads, each blade is equipped with strain gauges for flap and lead-lag bending in addition to the torsion strain gauge built into the blade. Figure 51 illustrates the neck of the blade which was fitted with pressure sensors. It shows the cables at the cable outlet (1), the flap (2) and lead-lag (3) strain gauges, some soldering terminals (4) and the blade shoe (5) with blade connector (6).

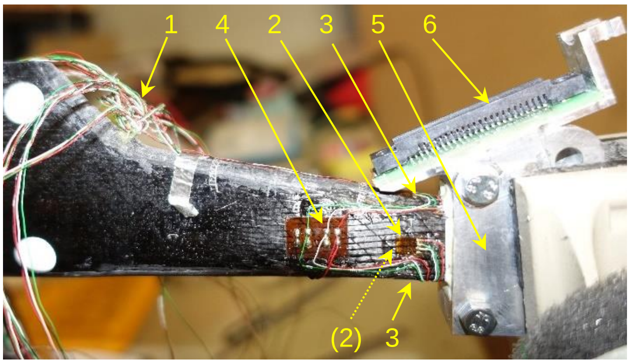

Figure 51: Blade neck prepared for cabling

The cables are sorted and gradually glued to the blade neck and led to the connector. Figure 52 depicts the cables laid on the upper side. It looks very similar on the opposite side.

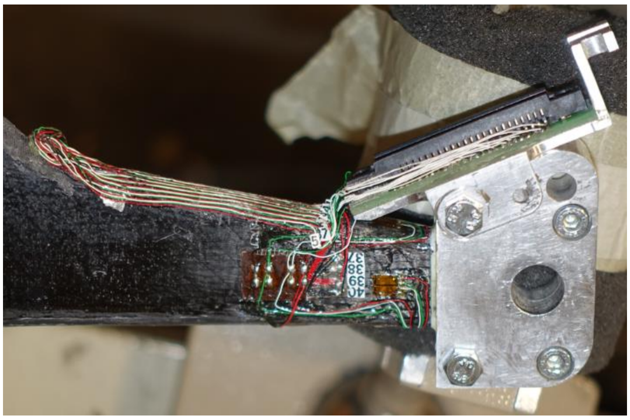

Figure 52: Blade root wiring

5. Blade root load test

Before the production of the series blades began, a load test was carried out on the highly loaded blade neck area of a pre-series blade. Figure 53 shows the test setup with the blade segment (1, equipped with strain gauges), the load application at the top with pull rod (2) and at the bottom (3) and the test machine clamps (4).

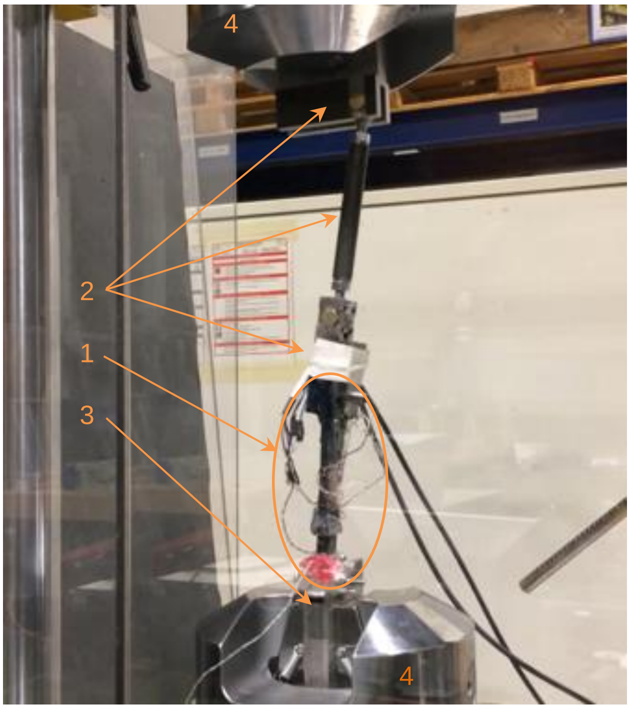

Figure 53: Rotor blade segment testing setup

Two start-up tests with 100,000 load cycles each were carried out. It is pulled diagonally so that the desired flap and lead-lag moments are created in addition to the pulling force. The target load of the first cycle corresponds to fast forward flight at rated rotor rpm. The second cycle represents fast forward flight at 15% higher rotor speed. In addition, for both test cases, a 10% load increase was given. The test machine required a certain initial test load, so that both tests were started with 680 N preload. Table 3 shows the maximum loads that were applied to the blade segment.

Table 3: Maximum loads in the load test

Test-case	"centrifugal load" [N]	flap moment [Nm]	Lead-lag moment [Nm]
1	6800	0 up to 21.6	0 up to 43
2	8060	0 up to 41.7	0 up to 39.6

The blade neck, loop and blade shoe withstood the two load tests without damage. Only the areas exposed to high loads (1) show a certain amount of wear as can be seen in Figure 54.

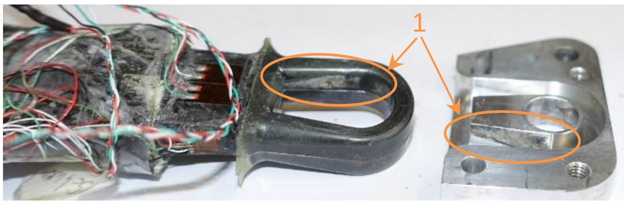

Figure 54: Blade root and shoe inspection

The component test thus confirmed the strength calculation and the serial blades were produced.

6. RESULTS

6.1. Optical assessment

After the final finishing and pre-tests at a whirl tower, the rotor blades are ready for use. The surface finish of the blades is good. For the wind tunnel test, the blades were not repainted, only partly polished. Figure 55 shows an enlarged view of the blade skin with two chimneys of pressure sensors.

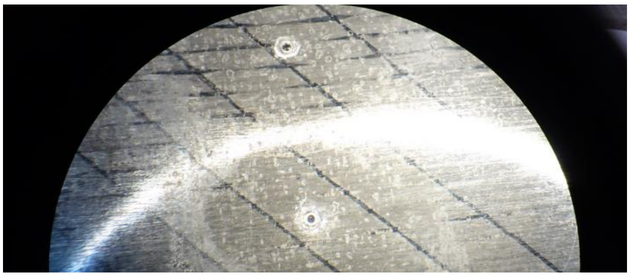

Figure 55: Skin surface with two pressure sensor chimneys

6.2. Instrumentation and LED

All strain gauges as well as the LED work properly. Amongst the 14 Kulites installed at 70% blade radius, 13 work properly. Figure 56 shows a blade tip with illuminated LED.

Figure 56: Blade tip with LED

6.3. Basic blade properties

Comparing the basic properties of all blades, very similar results can be found. A summary is listed in Table 4. As can be seen, the maximum mass deviation is about 5.5 g while the center of gravity and static moments are comparable.

Table 4: Basic properties of rotor blades

Blade No.	#1	#2	#3	#4
Mass / g	242.7	236.2	238.0	240.1
cg_R / R	43.0%	42.8%	42.9%	43.1%
cg_C / c	27.6%	27.1%	27.9%	27.9%
Static moment *) /Nmm	832	805	813	824

*) Bending moment of the blade around the rotor center under the influence of gravity.

Looking at the structural properties, all blades show very similar eigenfrequencies, as shown in Figure 57. The results were determined by a non-rotating ground vibration test, where each blade was clamped in a chuck. Only blade #1 has slightly lower eigenfrequencies, which can be explained by the higher mass and the lower stiffness because of the pressure sensors installed. The comparison with the design properties shows that all frequencies except that of the first torsion mode are a bit lower than expected but within the range for a safe rotor operation.

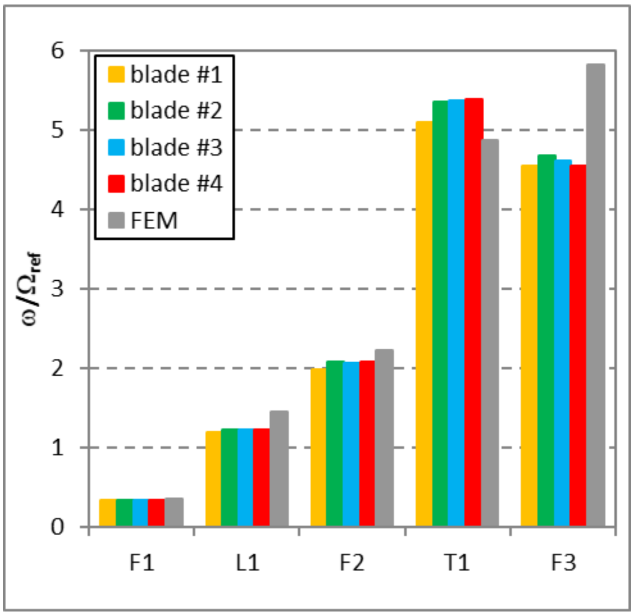

Figure 57: Rotor blade eigenfrequencies

7. SINGLE BLADE TEST

Before mounting the complete rotor system, each rotor blade was tested individually in the DLR whirl tower facility. For this purpose, a special rotor head was designed to mount a rotor blade on one side and a counter weight on the other side, as shown in Figure 58. Using a screw drive system, manual pitch angle changes are possible to set different angles of incidence. The main drive of the test rig is based on a 47 kW electric motor and a belt drive system. It was modified to reach a maximum rotor speed of 3000 rpm by exchanging the pinion and the belt.

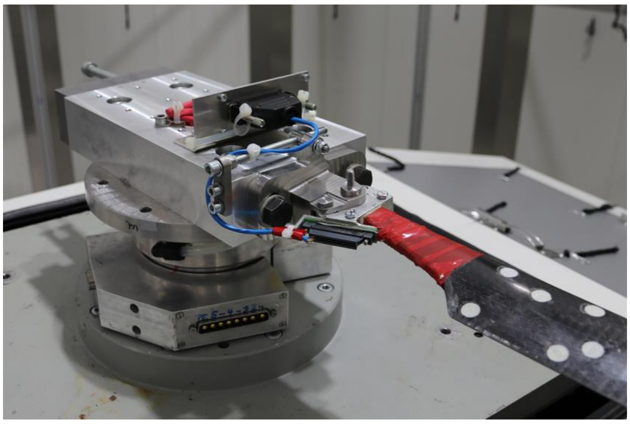

Figure 58: Rotor hub of whirl tower test rig

After the rotor balancing procedure, each rotor blade was driven to a rotor speed of 2500 rpm, which means about 120 % of nominal centrifugal load, since the rotor radius is increased by about 100 mm at this test rig. Each blade was tested at two different angles of incidence (+3 deg, +8 deg). All blades could be tested with the same counter weight.

To monitor the blade loads, the blade flap bending, lead-lag bending and torsion moment was measured using a direct connection of the strain gauge bridges with an amplifier via a small slip-ring system below the rotor system. Comparing the flap bending, lead-lag bending and torsion moments of the four rotor blades, a very similar behavior was found over rotor speed. Figure 59 shows the lead-lag bending moment as an example, where lag is positive. Here, a negative moment (lead) could be observed, resulting from a center of gravity of the blade which is located behind the tension axis. Blade #1 and #3 show a slightly higher moment, probably caused by the different mass distribution due to pressure sensor instrumentation (Blade #1) or a slightly different lag angle. All four rotor blades finally passed the whirl tower test successfully and were ready to be used in the complete rotor configuration.

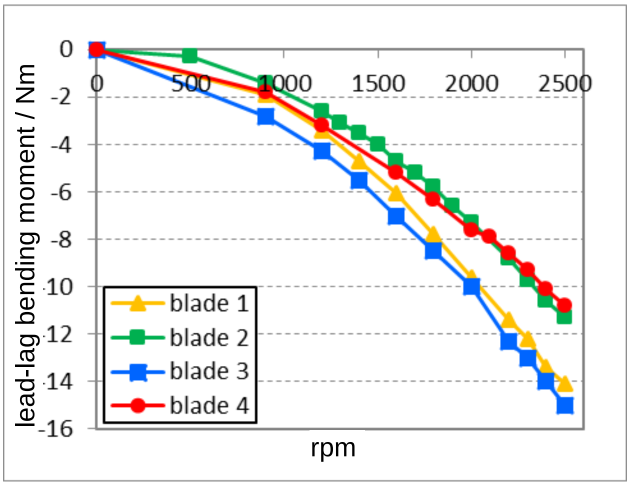

Figure 59: Lead-lag bending moment vs. rotor speed

8. BLADE SET TEST

After the individual blade tests, the four blades were mounted to the rotor test rig (Figure 60).

Figure 60: Overall rotor pre-tests in the rotor hall

The rotor was slowly accelerated to a speed of 500 rpm with a blade angle of 3° at 70 % blade radius. A first balancing was made at this speed. Then the speed was gradually increased until the nominal speed of 2481 rpm was reached. The balancing of the rotor was checked at each step and, if necessary, adjusted with weights attached to the blade mounting bolts.

The balance was checked at each step and adjusted if necessary. The tracking was also adjusted several times until the rotor finally ran smoothly. Finally, a thrust sweep was carried out and cyclic pitch angles were set to check the reaction of the rotor system. The rotor behaved very well in every aspect, so that it was ready for the wind tunnel test.

9. CONCLUSION AND OUTLOOK

• DLR Braunschweig has conducted wind tunnel tests for decades with whole helicopter model configurations and new model rotor blades. The dynamic design of rotor blades is well-known. Experiences with the treatment of composite material have also existed for a long time.

• A new rotor test rig with a rotor diameter of 1.624 m was designed and built at the DLR in Braunschweig. This also included the design and construction of the rotor blades. For the whole design process of Mach scaled model rotor blades, a multidisciplinary design chain was developed and established at DLR to satisfy all boundary conditions for save operations in wind tunnel experiments.

• The blade structure corresponds to that of the FTK blades (r = 2 m). The blade construction method was established for the FTK blade and has now been transferred to a significantly smaller scale (blade radius 0.812 m). Once again, the skins were produced using the Resin Transfer Molding process. When assembling the blades, the roving tapes required for the spar were impregnated with resin and processed. The blades contain prefabricated milled foams and nose mass caps.

• A particular challenge was the integration of 14 pressure sensors in one section and their cabling due to the limited space available.

• Essential for the success of the project was again the decision to use a cold curing and a stepwise manufacturing process for the rotor blades. This avoids difficulties with thermal expansion effects between the mold and the composite materials. On top of that, the tooling requirements are comparably small.

• A high-quality rotor blade set was produced. For the first time, a rotor blade of this size was successfully fitted with pressure sensors in a section using the selected manufacturing process. The manufacturing process presented has demonstrated its suitability and will be used for the production of future rotor blades. Depending on the size of the rotor blade, an instrumentation with significantly more pressure sensors is feasible.

• The rotor and the helicopter successfully completed the wind tunnel test that took place in June. Now the evaluation of the data obtained is underway.

10. REFERENCES

Reference 1: Mainz, H.; Bartels, R.; van de Kamp, B.; Kuntze-Fechner, G.; Hahn, M.: "*FTK Rotor Blades: Design, Manufacturing And Testing".* Proceedings of the 43rd European Rotorcraft Forum, September 12-15, 2017. Milan, Italy

Reference 2: van de Kamp, B.; Kalow, S.; Riemenschneider, J.; Bartels, R.; Mainz, H.: *"Multidisciplinary Design Chain for model rotor blades"*, ICAS September 25 – 30, 2016 - International Council of Aeronautical Sciences - Proceedings. Daejon, South Korea

Reference 3: Mainz, H.; van der Wall, B. G.; Leconte, P.; Ternoy, F.; Mercier des Rochettes, H.: *"ABC Rotor Blades: Design, Manufacturing And Testing"*. Proceedings of the 31st European Rotorcraft Forum, September 13-15, 2005. Florence, Italy

Reference 4: Schneider, O.; Mainz, H.; Brehl, E.; Henseleit-Wieser, S.; van der Wall, B. G.: "*Development Of A New Medium Size Helicopter Wind Tunnel Model"*. Proceedings of the 50th European Rotorcraft Forum, September 10-12, 2024. Marseille, France

Reference 5: Beaumier, P., Costes, M., Gavériaux, R.: *"Comparison Between FP3D Full Potential Calculations And S1 Modane Wind Tunnel Test Results On Advanced Fully Instrumented Rotors"*. Proceedings of the 19th European Rotorcraft Forum, September 14-16, 1993. Cernobbio, Italy

Reference 6: Becker, F., Kalow, S., Bartels, R., van de Kamp, B.: *„Automatisierte Dimensionierung der inneren Struktur und der Eigenfrequenzen von Hubschrauberrotorblättern im Hinblick auf eine automatisierte Rotorblattoptimierung."* Deutscher Luft- und Raumfahrtkongress, September 13-15, 2022. Dresden, Germany